



# The Diurnal Evolution of Cold Fronts in the Australian Subtropics

Gerald L. Thomsen<sup>a\*</sup> Michael J. Reeder<sup>b</sup> and Roger K. Smith<sup>a</sup>

<sup>a</sup>*Meteorological Institute, University of Munich, Germany*

<sup>b</sup>*School of Mathematical Sciences, Monash University, Australia*

## Abstract:

The effect of the diurnal cycle on the evolution of cold fronts in the Australian subtropics is investigated in two high-resolution numerical simulations. The simulations are made using the Pennsylvania State University/National Center for Atmospheric Research Mesoscale Model (MM5) with the initial and boundary conditions taken from the operational analyses of the European Centre for Medium Range Weather Forecasts. These simulations are compared with the observations of two cold fronts taken during the Central Australian Fronts Experiment in 1991. The simulations show a number of features that have been suspected, but never confirmed or quantified. (i) Although the wind field in the boundary layer is frontogenetic, daytime turbulent mixing is strongly frontolytic, which accounts for the weakening and deceleration of the fronts during the late morning and afternoon when convective mixing in the boundary layer is most vigorous. (ii) When the mixing subsides in the early evening, the low-level winds increase along with the deformation and convergence, leading to a strengthening and acceleration of the fronts. (iii) Bore-like disturbances are generated during the early hours of the morning as the nocturnal inversion strengthens. These bores propagate ahead of the front, developing a series of large-amplitude waves at their leading edge.

Copyright © 2008 Royal Meteorological Society

KEY WORDS Bore; Cold Front; Diurnal Cycle; Morning Glory; Sea Breeze

Received June 2, 2008; Revised ; Accepted

## 1 Introduction

Except during the warmest months (December to March), mid-latitude cold fronts in the Southern Hemisphere regularly extend far in to the subtropics (Reeder and Smith 1998). These subtropical incursions are most common during the dry season, but become less frequent as the continent warms and the mean subtropical ridge axis and mid-latitude westerlies migrate polewards. In the decade commencing 1988, a series of four, relatively modest field experiments were conducted in central and northern Australia to investigate the structure and behaviour of continental cold fronts as they advance into the subtropics. In total, fifteen fronts were documented in some detail during these experiments (Smith and Ridley 1990, Smith *et al.* 1995, Reeder *et al.* 1996, Deslandes *et al.* 1999, Reeder *et al.* 2000; Preissler *et al.* 2002), with the principal findings as follows.

- Cold fronts in the Australian subtropics are generally no deeper than about 1 km and they advance into a convectively well-mixed boundary layer, typically 3–4 km deep, which, during the night, overlies a strong, shallow radiation inversion.
- The fronts weaken and decelerate after sunrise as the mixing in the boundary layer intensifies.

- The fronts strengthen and accelerate in the evening as the boundary layer turbulence weakens: of the 15 fronts observed in during the field experiments, 13 crossed central Australia during the evening or early hours of the morning.
- As the fronts approach the northern coastline of the continent they invariably generate propagating bores in the evening or early hours of the morning. These bores propagate ahead of the front on the strong surface-based nocturnal inversion or on the cool air advected inland by the sea breeze. Over land, the bores generally dissipate before noon, by which time the stable layer is destroyed by convective mixing, but they decay much more slowly once over the water. If the air is moist enough, the bore waves generate lines of low cloud, known in Australia as morning glories, in this case southerly morning glories as there are other ways that bores can be generated over northeastern Australia (Smith 1988).

The present paper aims to explain these observations and to quantify the effects of the diurnal cycle within the convective boundary layer on their dynamics. A further aim is to examine the extent to which the fine-scale structure of fronts, including the bores they generate, can be forecast. Our study is focussed on numerical simulations of two cold fronts observed during the 1991 Central Australian Fronts Experiment (hereafter referred to as CAFE91). These fronts are selected as they are

\*Correspondence to: Michael J. Reeder. School of Mathematical Sciences, Monash University, Australia. E-mail: michael.reeder@sci.monash.edu.au



typical of the fifteen observed and they are relatively well documented. Even so, despite the additional field data, the observational data over central and northern Australia are still comparatively sparse and the fronts are not sampled well enough to provide a complete picture of their structure and evolution. Therefore, our approach is to use the numerical simulations to fill the gap and provide a more complete picture of the fronts and the bore-like disturbances that they generate on spatial scales much finer than the observational network. (See Smith *et al.* 1995 for further information on the observational network deployed for CAFE91.)

The only previous investigations into the effect of the diurnal cycle on the dynamics of cold fronts that we are aware of have been idealised and focussed on the midlatitudes (Pagowski and Taylor 1998, Reeder and Tory 2005). One other study by Thomsen and Smith (2006) examined the generation of propagating bores by cold fronts. They analysed simulations of two southerly morning glories generated by cold fronts observed during the Gulf Lines EXperiment (GLEX) in 2002. (The results of GLEX are reported by Goler *et al.*, 2006, Smith *et al.*, 2006 and Weinzierl *et al.* 2007.) The present study differs from that by Thomsen and Smith by its focus on the dynamics of cold fronts in the Australian subtropics, whereas Thomsen and Smith were concerned mainly with the prediction and evolution of the bore associated with the southerly morning glory. Consequently, the present work compliments that by Thomsen and Smith.

The simulations described are made using the Pennsylvania State University/National Center for Atmospheric Research Mesoscale Model (MM5), with the initial and boundary conditions provided by the operational analyses from the European Centre for Medium Range Weather Forecasts (ECMWF). The horizontal grid resolution of the inner domain is 3 km, which is much smaller than that currently used for numerical weather prediction. Apart from Thomsen and Smith (2006), all previous modelling work on subtropical cold fronts has been based on operational numerical weather prediction output with horizontal resolutions no better than 50 km (Smith *et al.* 1995, Deslandes *et al.* 1999, Reeder *et al.* 2000; Preissler *et al.* 2002).

The paper is structured as follows. Section 2 summarises the numerical model and initial conditions. Sections 3 and 4 discuss the numerical simulations of the two best observed cold fronts during CAFE91, comparing the simulations against the available observations. Both cases are relatively well documented examples of nocturnal frontogenesis and the associated generation of propagating bores. The first case, Event 1, is included as it provides a clear example of how fronts in the Australian subtropics weaken and stall during the day, but develop sharp surface wind changes after sunset. Although the temperature contrast is relatively weak in Event 1, the cold front generated a bore which separated from the front. In contrast, the second case, Event 2, is a strong nocturnal front marked by sharp temperature falls. It is included as the

bore generated remains attached to the cold front throughout most of the early morning. Once the front begins to weaken, the bore propagates far ahead of the original cold front and develops into the principal wind change. The structure of the bores in each event is discussed in Section 5, while some conclusions are drawn in Section 6.

## 2 MM5

MM5 is described in detail by Grell *et al.* (1995). The model is nonhydrostatic and uses a finite difference approximation to the equations with  $\sigma = (p - p_t)/(p_s - p_t)$  as the vertical coordinate, where  $p$  is pressure,  $p_s$  is the surface pressure and  $p_t$  the top pressure, set here to 100 mb. There are 23  $\sigma$ -levels with 15 levels below 3 km. The latter are located at heights of approximately, 0, 40, 80, 150, 230, 300, 380, 540, 700, 870, 1200, 1550, 1900, 2300 and 2750 m, giving a relatively high resolution in the boundary layer.

The calculations are made on two nested, horizontal domains. The locations of these domains are plotted in Fig. 1. The outer domain has  $221 \times 221$  grid points with a horizontal resolution of 9 km and the inner domain has  $361 \times 361$  points with a horizontal resolution of 3 km. The land use and orography are taken from the MM5 data set and have a 5' resolution for the outer domain and 2' resolution for the inner domain. The time step is 27 s for the outer domain and 9 s for the inner domain. The Grell cumulus parameterization scheme (Grell 1993) is implemented in the outer domain, but no cumulus scheme is used in the inner domain as cold fronts over central and northern Australia are mostly dry. The boundary-layer scheme as implemented in the National Centers for Environmental Prediction (NCEP) Medium Range Forecast (MRF) system by Hong and Pan (1996) is selected for all domains. The Dudhia scheme (Dudhia 1989) is chosen to represent explicit moisture conversions, and a bucket scheme is used for the soil moisture budget. A short and long-wave cloud and ground radiation scheme that takes account of diurnal variations is used. A wave radiation scheme is applied at the upper boundary to inhibit the reflection of wave energy from the model top. The initial conditions for the two cold fronts examined here are taken from the ECMWF operational analyses at 1000 Eastern Standard Time (EST) on 9 September and 16 September. (EST = UTC + 10 h.) These data have a horizontal resolution of  $0.25^\circ$ . In each case the model is integrated forward for 48 h.

## 3 Event 1

Event 1 developed a sharp wind change during the night of 9-10 September, arriving at Mount Isa, which is close to the centre of both model domains, at about 0930 EST 10 September. (All places mentioned in the text are marked in Fig. 2.) The passage of the front raised dust across the region, which lasted throughout most of the morning and closed the airport at Mt Isa. Despite the strength of the wind change, only weak temperature falls were recorded

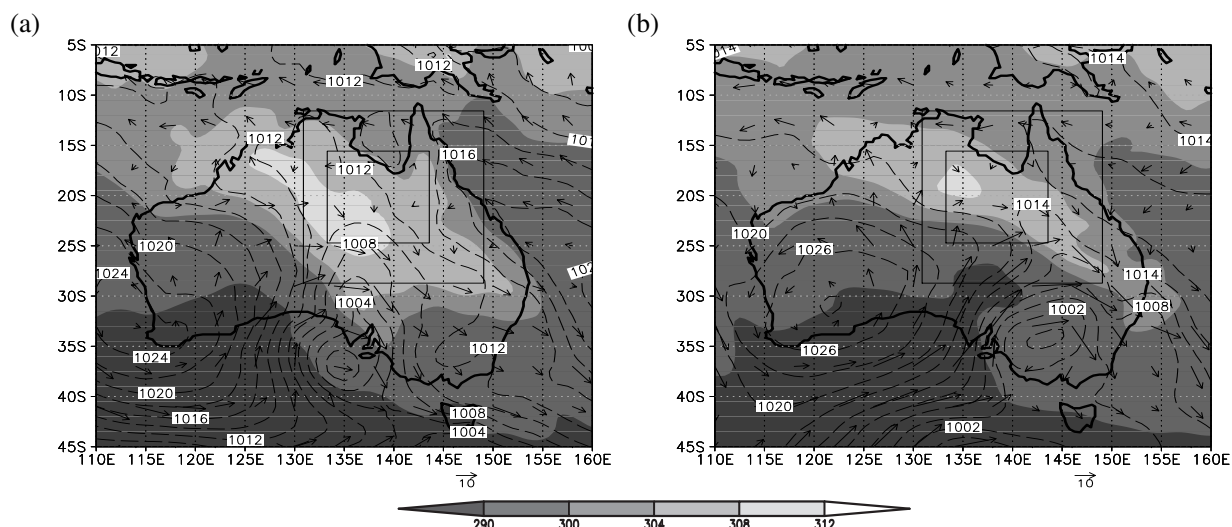


Figure 1. Event 1. ECMWF analyses at (a) 1600 EST 9 September and (b) 1000 EST 10 September. MSLP (dashed lines), horizontal wind vectors and virtual potential temperature (shaded) at 850 mb. Contour intervals are 3 mb and 4 K. The two boxes centred over northeastern Australia show the outer and inner domains used in the simulations with MM5.

at the surface. The front weakened further and stalled during the day. It subsequently reformed and accelerated, passing through Hughenden (144.2°E, -20.8°S) in the eastern most part of the domain at about 2330 EST 10 September.

### 3.1 Synoptic environment for Event 1

The synoptic environment for Event 1 is illustrated in Fig. 1, which shows the ECMWF analyses of mean sea level pressure (MSLP) at 1600 EST 9 September and 1000 EST 10 September. Horizontal wind vectors and the virtual potential temperature at 850 mb are plotted also. In mid afternoon (1600 EST) on 9 September, a low pressure system lying over the ocean just south of the continent is connected to a trough extending northward and westward. The warmest air lies along the northwestern part of the trough. This thermal ridge and its associated pressure trough will be called simply the heat trough. An anticyclone is located to the west of the low and associated trough, and at low levels the wind is directed across the isobars towards the trough. A ridge extends along the northeastern coastline, directing an onshore flow. The cold front (Event 1) is characterised by the largest virtual potential temperature gradient and is oriented southeast to northwest from the northern part of the low and along the northeastern boundary of the high. This synoptic pattern, with the cold front lying in the trough region between two anticyclones and relatively far from the center of the low, is the predominant synoptic environment for cold frontal passages across Australia (Reeder and Smith 1998).

By mid-morning the following day (1000 EST 10 September) the cold front has strengthened, the heat low has contracted, and they have both moved northeastward (Fig. 1b). Overnight strengthening, as illustrated in Fig. 1, is the norm for fronts as they advance across the Australian interior (Reeder and Smith 1998). The low is now located in the southeastern corner of the continent

and the high has expanded across much of the western and central parts of Australia. The configuration of the high and low directs southwesterly winds across much of central Australia. On the northeastern side of the front the flow is northwesterly, while on the southwestern side it is southwesterly.

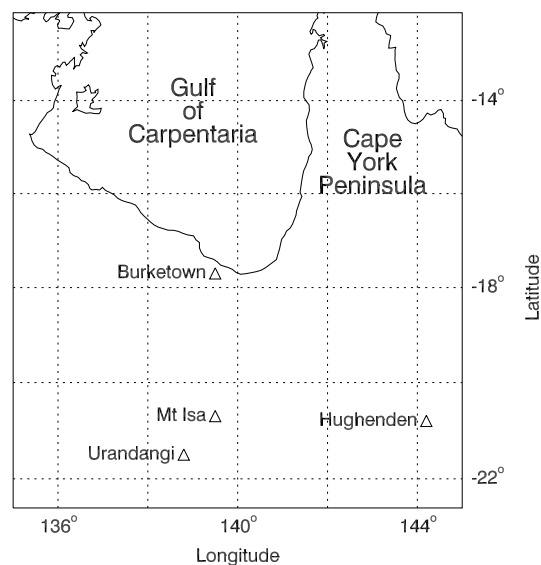


Figure 2. Map of northeastern Australia marking the places mentioned in the text.

### 3.2 Mesoscale structure and evolution of Event 1

The mesoscale structure and evolution of Event 1 in the 24 hr period commencing 1500 EST 9 September is examined now. The potential temperature, horizontal wind vectors and cyclonic relative vorticity from the outer grid

of the MM5 simulation are shown in Fig. 3 at six hourly intervals.

During the afternoon (1500 EST 9 September, Fig. 3a), the dominant feature is the heat trough, which is oriented northwest to southeast and lies in the western half of the domain. The wind change across the heat trough is relatively weak. The cold front, identified by the line of strongest gradient in potential temperature, is located in the southwestern corner of the model domain and is separate from the heat trough (see also Fig. 1a). In the northern part of the domain, coastal gradients in the potential temperature mark the leading edges of the sea breeze fronts. At this time the sea breeze fronts are confined to the coastal margin, with the exception of the east coast of the Cape York Peninsula where the background easterlies have advected the sea breeze front inland.

Six hours later at 2100 EST (Fig. 3b) the front has advanced northeastwards into the model domain, although the position of the trough axis, as defined by the maximum relative cyclonic vorticity, has not moved appreciably. Nevertheless, the winds have strengthened significantly both ahead of and behind the trough, and the cold front and heat trough have become indistinguishable. To the south of the trough the wind is strong (typically  $20 \text{ m s}^{-1}$  on the  $0.955 \sigma$  surface) and southwesterly, while on the northern side it is weaker and northerly or northwesterly. The southwesterlies behind the front are associated with the ridging across the continent (Fig. 1a) and are accompanied by the northeastward progression of the cooler air. At this time, the sea breeze front has advanced about 150 km inland from the gulf coast.

By 0300 EST 10 September the cold front is well marked by the relatively strong gradient in potential temperature and a pronounced line of cyclonic relative vorticity, oriented northwest to southeast, in the southwestern part of the domain (Fig. 3c). One of the most important features of the simulation is that the winds strengthen and turn anticyclonically throughout the night. The anticyclonic rotation is especially pronounced in the cold air on the southwestern side of the trough. The overnight acceleration of the low-level winds and subsequent intensification of the cold front are evidently related to the way in which the boundary layer adjusts to large changes in the turbulent stress. Although not shown here, the winds in the boundary layer are sub-geostrophic during the day because of the stress associated with turbulent mixing. At night, once the (buoyantly-generated) turbulent mixing subsides, the balance of forces in the boundary layer is dramatically altered. In response, the wind rotates anticyclonically and air parcels accelerate down the pressure gradient towards the trough, strengthening the low-level flow. Inertial oscillations such as these are a common feature of the boundary layer over the Australian interior (e.g. May 1995; Arnup and Reeder 2007).

The cold front continues to advance northwestward, and by 0900 EST (Fig. 3d) it is close to Mt Isa as observed. However, in the following 6 hours (1500 EST Fig. 3e),

the structure of the front changes dramatically. The low-level winds weaken as the daytime turbulent mixing in the boundary layer increases. A curved line of cyclonic relative vorticity still marks the leading edge of the cold front, but the potential temperature gradients in the cold air are mostly weaker than at 0900 EST and the cold front is stationary. The isentropes near the leading edge of the front are more convoluted than they were six hours earlier as a result of the vigorous daytime mixing and the underlying topography. Consequently, in some localised regions the horizontal potential temperature gradient is a little stronger than before. By this time the heat trough has become re-established in the westernmost part of the domain.

### 3.3 Frontogenesis during Event 1

The material rate of change of the magnitude of the horizontal potential temperature gradient,  $|\nabla_h \theta|$ , was introduced by Petterssen (1936) as a measure of the tendency of the atmosphere to develop fronts (see also the generalization by Keyser *et al.* 1988) and is known as the frontogenesis function. In sigma coordinates on the sphere, the frontogenesis function can be expressed as

$$\begin{aligned} \frac{D}{Dt} |\nabla_h \theta| &= -\frac{1}{2} |\nabla_h \theta| (D - E' \cos(2\beta)) \\ &\quad - \frac{\partial \theta}{\partial \sigma} \mathbf{n} \cdot \nabla_h \dot{\sigma} + \mathbf{n} \cdot \nabla_h \dot{Q} \end{aligned} \quad (1)$$

where  $\theta$  is the potential temperature,  $\dot{Q}$  is the diabatic heating rate, which includes radiative effects, latent heating, turbulent mixing and thermal diffusion,  $\mathbf{n} = \nabla_h \theta / |\nabla_h \theta|$  is the unit vector pointing along the potential temperature gradient towards warmer air,  $D = \partial u / \partial x + (\partial(v \cos \varphi) / \partial y) / (\cos \varphi)$  is the horizontal divergence,  $E = \partial u / \partial x - (\cos \varphi) \partial(v / \cos \varphi) / \partial y$  is the stretching deformation,  $F = \partial v / \partial x + (\cos \varphi) \partial(u / \cos \varphi) / \partial y$  is the shearing deformation,  $E' = \sqrt{E^2 + F^2}$  is the total deformation,  $\varphi$  is the latitude,  $x$  is the arc length along a line of constant latitude,  $y$  is the arc length along a line of constant longitude,  $\alpha = \tan^{-1}((\partial \theta / \partial x) / (\partial \theta / \partial y))$ ,  $\delta = \frac{1}{2} \tan^{-1}(E / F)$  is the angle between the  $x$  axis and the axis of dilatation, and  $\beta = \delta - \alpha$  is the angle between the axis of dilatation and the isentropes.

Physically, the first term on the right hand side of Eq. (1) describes the contribution to material rate of change of the horizontal potential temperature gradient from the combined effects of convergence and deformation. The second term represents the contribution due to the tilting of vertical gradients of potential temperature into the horizontal, while the third term is the contribution from differential diabatic heating in the direction of the potential temperature gradient.

Figures 4a and 4b show vertical cross sections of the frontogenesis function calculated on the outer domain at 2100 EST 9 September and 1500 EST 10 September respectively. These times correspond with Figs. 3b and 3e and are chosen to illustrate the differences in the structure and evolution of the cold front at night and during the day.

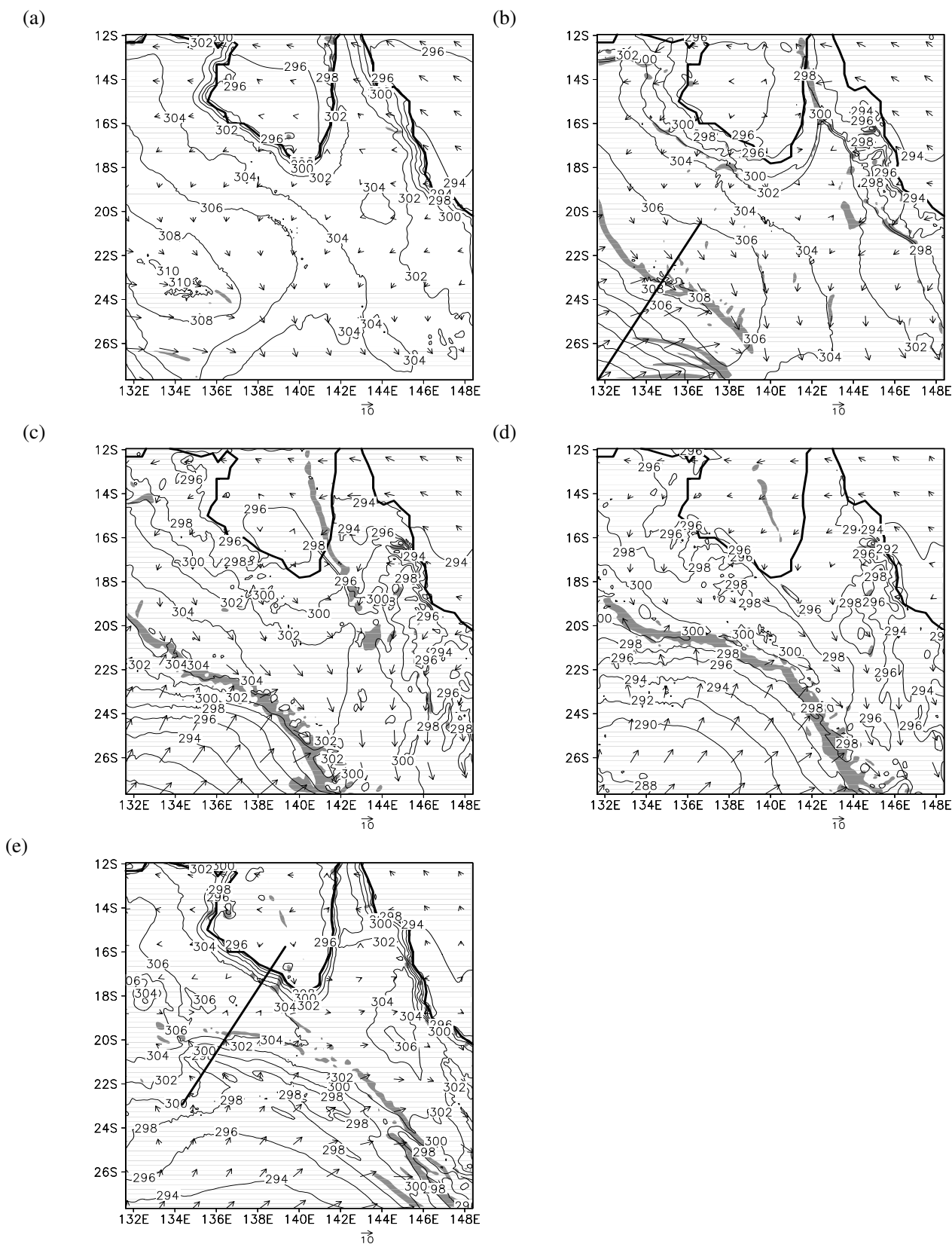


Figure 3. Event 1. Potential temperature and horizontal wind vectors on the  $\sigma = 0.955$  surface from the MM5 outer domain at (a) 1500 EST 9 September, (b) 2100 EST, (c) 0300 EST 10 September, (d) 0900 EST and (e) 1500 EST. Contour interval for potential temperature is 2 K. The arrow below each panel indicates  $10 \text{ ms}^{-1}$ . Shading marks those regions where the magnitude of the cyclonic relative vorticity exceeds  $7.5 \times 10^{-5} \text{ s}^{-1}$  on the same  $\sigma$ -surface. The thick lines in panels b and e mark the location of the vertical sections plotted in Fig. 4.

The location of the cross sections are marked on Figs. 3b and 3e. Figures 4c and 4d show the contributions to the frontogenesis function from the convergence and deformation terms at the two times. The tilting terms contribute relatively little to the frontogenesis function and are not plotted. The contribution by differential diabatic heating to the frontogenesis function, plotted in Figs. 4e and 4f, shows a great deal more local variability than the deformation and convergence terms as it appears to be linked more closely to the variations in the topography, boundary layer eddies and the thermodynamic and radiative effects of cloud. For this reason, the fields of frontogenesis have been smoothed in the horizontal and vertical directions using a 9 point filter. Even after smoothing the frontogenesis fields show considerable spatial variability as the pattern of underlying topography, the daytime turbulent mixing and the attempt of the model to produce boundary layer rolls are imprinted strongly on the low-level winds and potential temperatures, and also because the calculation of the frontogenesis function involves products of differentiated quantities. The background field in all panels of Fig. 4 is the potential temperature.

During the late evening at 2100 EST, the surface wind change is located at about 600 km in the plane of the vertical cross section. The cold air is relatively deep. For example, the 306 K isentrope slopes uniformly from the leading edge of the surface front to a height of about 4 km at the left hand edge of the cross section. The cold front advances into a deep well mixed layer overlying a very shallow radiation inversion. At this time above the lowest few hundred metres, the frontogenesis function is positive along the leading edge of the cold front and in the warm air ahead (Figs. 4a). The main region in which deformation and convergence contribute to frontogenesis is centred on the cold front, but there are other localised regions (Figs. 4c). Although not shown, the strong horizontal winds are confined to the lowest 2 km and develop once the daytime mixing ceases. It is for this reason that cold fronts in the Australian subtropics are shallow: cold fronts develop where there is active frontogenesis, which, in this case, is in the lowest 2 km of the atmosphere.

On the following day at 1500 EST the cold front and sea breeze front are located at about 400 km and 800 km respectively in the plane of the vertical cross section. During the day, buoyantly-generated turbulent mixing produces a broad heat trough between the cold front and the sea breeze front that is relatively homogeneous in the horizontal. The mixed layer ahead of the cold front is about 3 km deep, while in the cold air to the south of the front the mixed layer is 2 km deep. At this time, the frontogenesis function is negative at the leading edge of the front, although it becomes positive in the cold air (Figs. 4b). This pattern of frontolysis and frontogenesis accounts for the weakening and deceleration of the cold front during the day. A similar pattern occurs at the sea breeze front and is the reason why the front remains fixed to the coast during the day. The main contributions from deformation and convergence to the near-surface frontogenesis are found to the rear of the leading edge of

the cold front. While an increase in the turbulent stress in the boundary layer increases the cross-isobaric flow, it also decelerates the flow, the net result being a weaker field of deformation and convergence (Figs. 4d). Deformation and convergence are produced by the developing sea breeze circulation and are important also in strengthening the sea breeze front.

The differential diabatic heating term at the two times are shown in Figs. 4e and f. At night, the contribution to the frontogenesis function from differential diabatic heating is mostly negative. The main exception to this pattern is below the shallow cloud that forms in the prefrontal air. Here the longwave radiative emission by the cloud warms the air, while longwave radiative emission from the surface produces a shallow region of frontolysis in the lowest layers of the model. During the day solar radiation heats the surface, which then warms the air close to the surface. Subsequently, this heated air is distributed through the boundary layer by turbulent mixing. To the extent that the radiative heating is homogeneous, the mixed layer warms at a rate which is inversely proportional to its depth, and hence the pattern of daytime heating largely reflects the height of the mixed layer. Consequently, the cold side of the front warms faster than the warm side as the mixed layer is shallower in the cold air. This pattern of heating and cooling is frontolytic also. These results are consistent with those of Reeder and Tory (2005) who found that, in a version of the Eady problem which included a boundary layer, differential heating produced by horizontal variations in the mixed-layer depth was frontolytic during the day.

#### 3.4 Comparison between the observations and simulation of Event 1 on the inner grid

The model calculations on the inner grid are compared now with the observed structure and evolution of Event 1 as it traversed northeastern Australia. Figure 5a shows a time-height cross section of potential temperature constructed from radiosonde ascents made hourly at Mount Isa around the time of passage of Event 1. Time in this figure runs from right to left so that, to the extent that a Galilean transformation from time to space is appropriate, the section approximates a vertical cross section through the front. Figure 5b shows the corresponding time-pseudo height cross section of potential temperature at approximately the location of Mount Isa constructed from the model simulation on the inner grid. (Pseudo-height is a pressure dependent height-like coordinate defined by Hoskins and Bretherton 1972).

The model captures the key features in the observations. In the early hours of the morning on 10 September, a shallow radiation inversion forms beneath a weakly stable remnant of the mixed layer from the previous day. Above the remnant mixed layer lies the more stable free atmosphere. Throughout the early hours of the morning the stable layer deepens, although the stable layer in the model is a little weaker than that observed. For example, at 0600 EST the observed stable layer is about 50 m

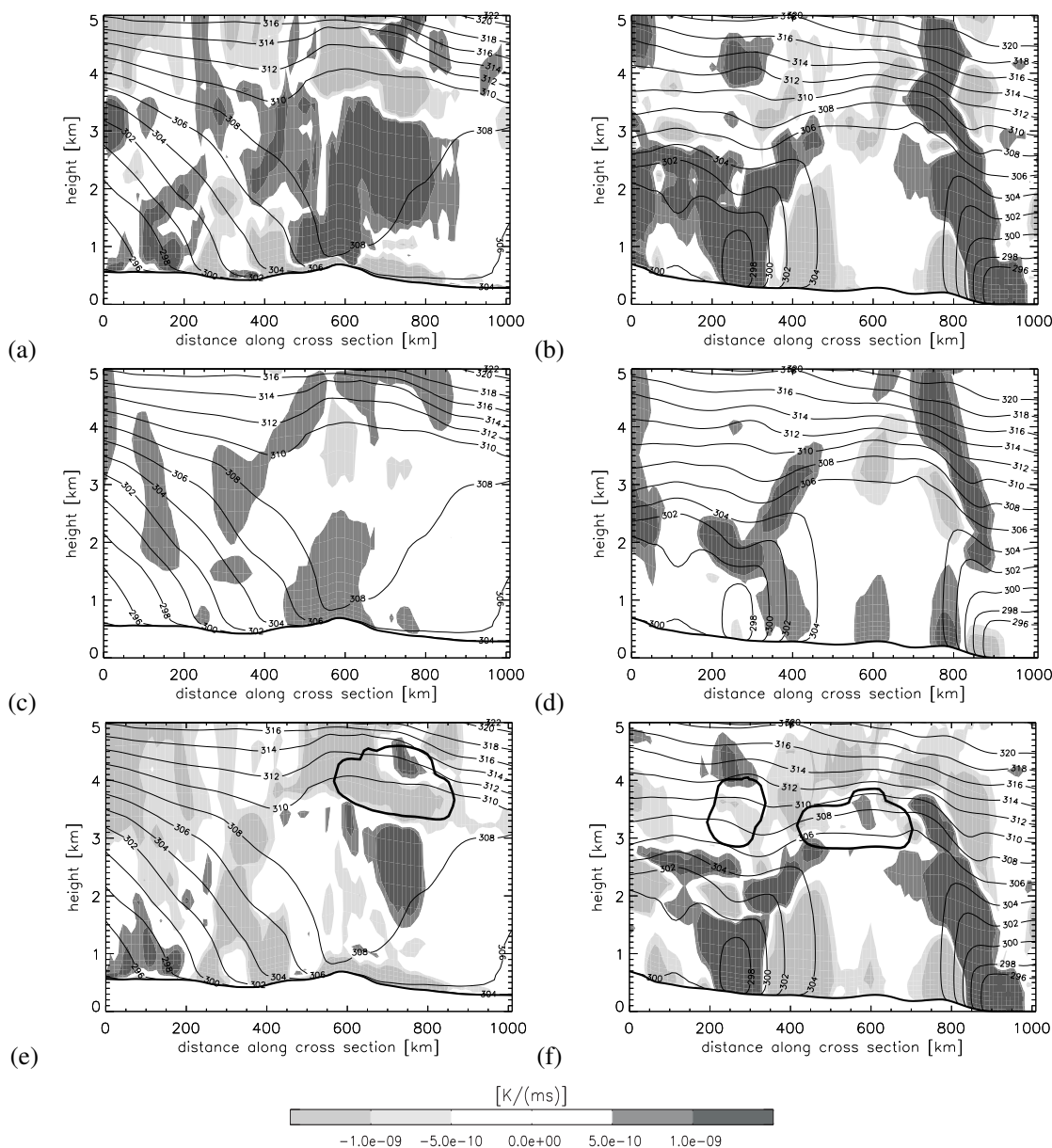


Figure 4. Event 1. Vertical cross section of the potential temperature and contributions to the frontogenesis function from the MM5 outer domain. Left hand side panels are at 2100 EST 9 September along the line marked in Fig. 3b. Right hand side panels are at 1500 EST 10 September along the line marked in Fig. 3e. (a)–(b) Frontogenesis function  $D|\nabla_h\theta|/Dt$ . (c)–(d) Convergence and deformation term  $-\frac{1}{2}|\nabla_h\theta|(D - E' \cos(2\beta))$ . (e)–(f) Differential diabatic heating term  $\mathbf{n} \cdot \nabla_h \dot{Q}$ . Contour interval for potential temperature is 2 K. Contour interval for frontogenesis is  $5 \times 10^{-10} \text{ K m}^{-1} \text{ s}^{-1}$ . In panels (e)–(f) the bold contours mark cloud.

deeper and the change in the potential temperature from the surface to the top of the stable layer is 2 K greater. Shortly after 0800 EST the mixed layer begins growing in both the observations and model, reaching a height in the mid-afternoon of nearly 3 km in the model compared with about 2 km in the radiosonde cross section. While the mixed layer in the model is much deeper than observed, the radiosondes show that the lapse rate is relatively small above the mixed layer, but not zero. In both the model and observations, the atmosphere is strongly stable above about 3.5 km and the mid-afternoon mixed-layer temperature is 304 K. Although the front arrives at 0930 EST, its passage is obscured by the daytime heating and associated mixing which opposes the local cooling from the

advection of cold air behind the front. The airmass change becomes apparent only after the diabatic heating and mixing begins to wane in the late afternoon. The inversion capping the cold air is more pronounced in the observations than in the model, which is a common limitation of numerical models which seldom have adequate vertical resolution to capture sharp inversions.

### 3.5 Development of the bore

The potential temperature, horizontal wind vectors and horizontal convergence from the inner grid of the MM5 simulation at 0600 EST 10 September are shown in Fig. 6. At this time, two curved convergence lines spaced

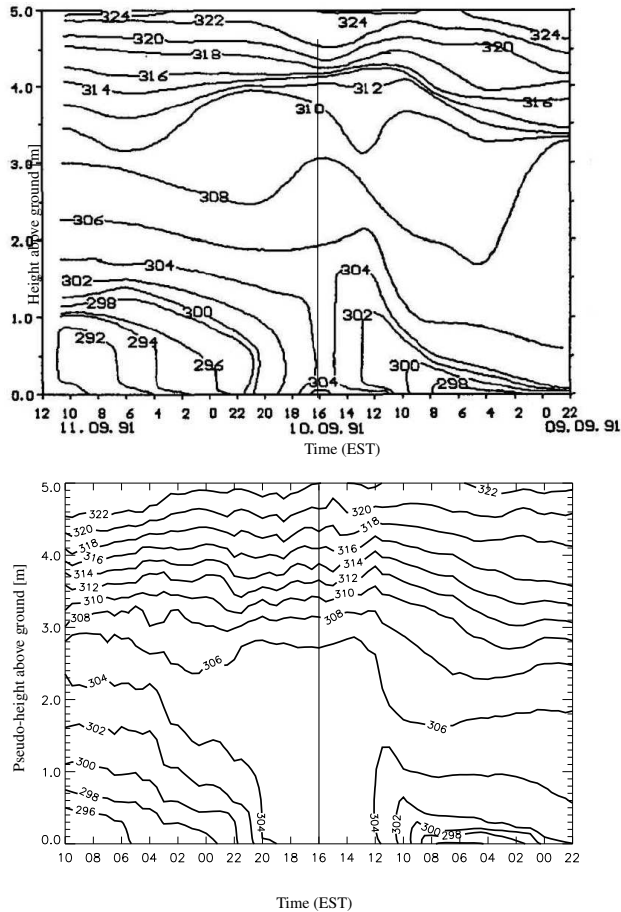


Figure 5. Event 1. (a) Time-height cross section of potential temperature from radiosonde ascents at Mt Isa. Time increases from right to left along the abscissa. The height in km is plotted along the ordinate. Contour interval is 2 K. Reproduced from Smith *et al.* (1995). The time of the frontal passage is indicated by a vertical line. (b) Time-height cross section of potential temperature from the MM5 inner domain. Contour interval is 2 K. Pseudo-height in km is plotted along the ordinate.

approximately 60 km apart lie across the inner model domain, extending from about 20°S in the western part to the southeastern corner. The wind ahead of the leading line is northwesterly, but backs and becomes westerly on the southern side. The wind backs again across the second line, becoming southerly in the colder air. The magnitude of the convergence varies considerably along the cold front, reflecting the variability in the boundary layer and underlying topography. Away from the front, short convergence lines aligned roughly parallel to the low-level winds appear to be attempts by the model to produce boundary layer rolls.

Figure 7 shows vertical cross sections of potential temperature, vertical motion and relative horizontal wind normal to the front on the inner grid at the same time as Fig. 6. The speed  $c$  is determined graphically by comparing position of the leading edge of the front at consecutive times, and the relative horizontal wind normal to the front is defined as  $u_n - c$ , where  $u_n$  is the horizontal wind in the plane of the cross section. The position of the vertical cross section is marked in Fig. 6. The structure of

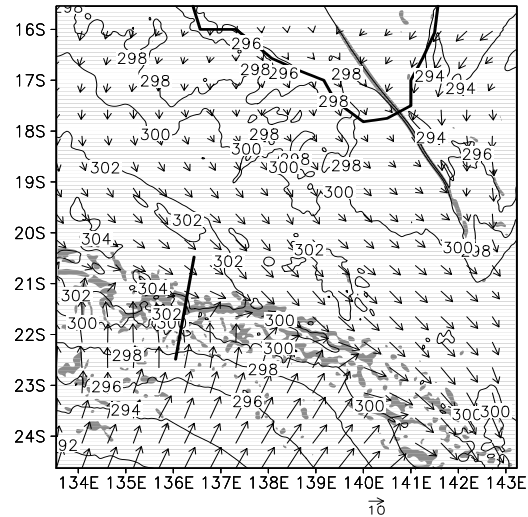


Figure 6. Event 1. Potential temperature and horizontal wind vectors on the  $\sigma = 0.955$  surface from the MM5 inner domain at 0600 EST 10 September. Contour interval for potential temperature is 2 K. The arrow below each panel indicates  $10 \text{ m s}^{-1}$ . Shading marks those regions where the horizontal convergence larger in magnitude than  $1.5 \times 10^{-4} \text{ s}^{-1}$  on the  $\sigma = 0.9975$  surface. The thick lines mark the location of the vertical section plotted in Fig. 7.

the two convergence lines identified in Fig. 6 is brought out more clearly in these cross sections.

The first change is located at 120 km, at which point the isentropes are displaced sharply upward. For example, the height of the 301 K contour changes abruptly by about 600 m. The change propagates to the right (downstream) into a low-level stable layer. To the left of the change (upstream), the change the low-level isentropes bulge upward before almost returning to their downstream height. This kind of structure is characteristic of a solitary wave. At the leading edge of the jump there is strong upward motion and a surge in the horizontal wind in the lowest 1 km. The second change is located at 80 km. Once again the isentropes are displaced upward. This time the 301 K contour changes by about 400 m and does not return to its upstream elevation. This sharp, permanent, isentropic displacement, is suggestive of a bore. On the upstream side of the jump, especially at heights above about 2 km, the isentropes have a wave-like structure, which is the defining characteristic of an undular bore. Atmospheric bores are invariably undular (Christie 1992). There is a strong updraught at the leading edge of the bore. The horizontal temperature gradient associated with both changes is very weak at the surface, which agrees well with Smith *et al.* (1995) who reported that, while Event 1 was characterized by a strong wind change, the temperature decreased little at the surface with the passage of the change. The simulation produces also a very strong low-level surge in the wind behind the second change, which gives rise to mechanically-generated turbulence and vigorous mixing in the cold air. The dynamics of the bore is discussed further in Section 5. In the NOAA-12 Advanced Very High Resolution Radiometer (AVHRR) visible satellite image at 0818 EST (Fig. 8), the leading

line appears prominently as a rope cloud. The satellite image shows also cloud lines in the cold air oriented perpendicular to the rope cloud with some similarity to the boundary layer rolls developed by the model.

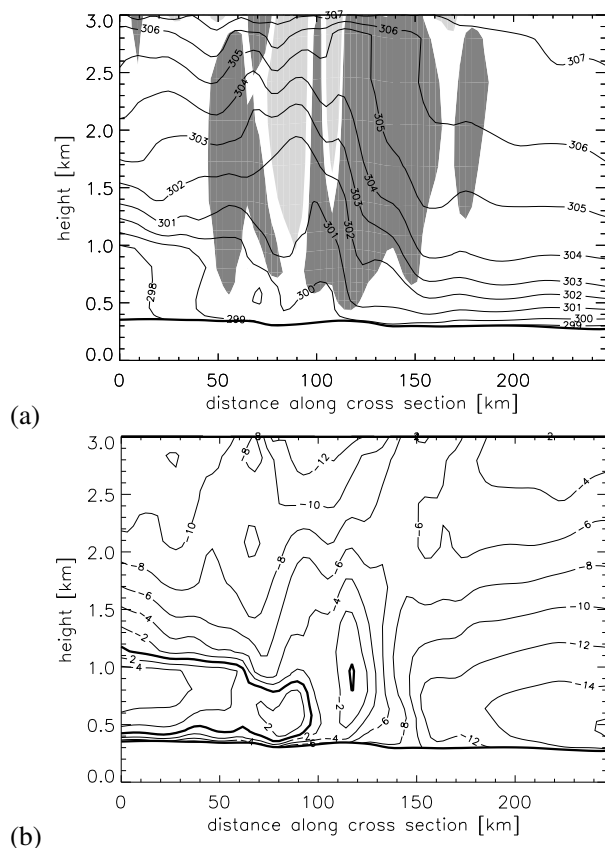


Figure 7. Vertical cross sections from the MM5 inner domain. Event 1 at 0600 EST 10 September. (a) Potential temperature and vertical motion. Contour interval for potential temperature is 1 K. Dark shaded regions represent vertical wind speeds greater than  $10 \text{ cm s}^{-1}$ . Light shaded regions represent vertical wind speeds less than  $-10 \text{ cm s}^{-1}$ . (b) Relative horizontal wind speed in the plane of the cross section  $u_n - c$ , where  $c = 11 \text{ m s}^{-1}$ . The bold line marks the  $0 \text{ m s}^{-1}$  contour.

A time-series of the surface observations taken at Urandangi between 0500 EST and 1100 EST on 10 September is plotted in Fig. 9a. The singular feature of the time-series, and a signature common to cold fronts over subtropical Australia, is the double change. The first change at 0700 EST is a propagating bore, the leading edge of which is marked by a pressure jump of 1.8 mb and a sharp change in wind direction from northwesterly to westerly. This change is followed by a series of pressure oscillations coinciding with fluctuations in the wind speed and direction. The wind and pressure signatures are typical of a series of amplitude-ordered solitary waves (Smith 1988, Christie 1992). The second change at 0815 EST marks the cold front. At this boundary the pressure rises slightly, the wind backs from westerly to southerly, and the wind speed increases notably. Both the dew-point temperature and mixing ratio (not shown) fall sharply with the second change. The dashed lines in Fig. 9a are the corresponding curves taken from the model

simulation. While the model produces two changes also (as shown in Figs. 6 and 7), the double structure is less apparent at the surface than in the observations. These time-series show a double change also with a pressure jump and wind change (speed increase and direction change) at 0600 EST followed by a further freshening of the wind, a wind direction change and a pressure rise commencing at about 0715 and finishing at about 0830 EST. The second change brings about a steady fall in dewpoint temperature, but little change in temperature.

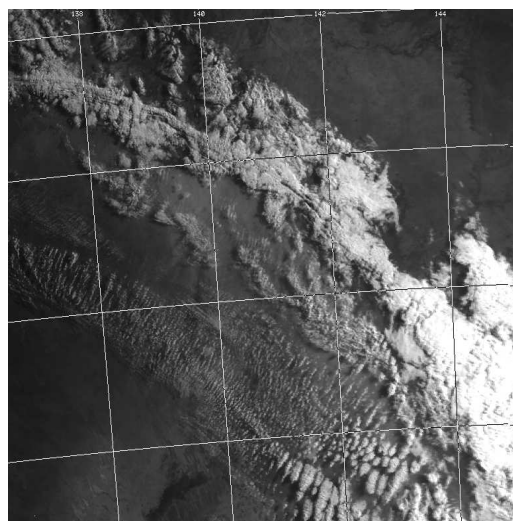


Figure 8. Event 1. NOAA-12 Advanced Very High Resolution Radiometer (AVHRR) visible satellite image at 0818 EST 10 September 1991. Reproduced from Smith *et al.* (1995).

While not central to the main themes of the paper, it is worth noting the series of convergence lines in the north-eastern part of the inner model domain in Fig. 6. These mark another bore, which has propagated southwestward into the domain from the middle part of the Cape York Peninsula where it was generated (see Figs. 3b-d). During the late dry season, southwestward propagating bores are commonly generated over the Cape York Peninsula in the late evening or early hours of the morning as the east-coast and west-coast sea breezes meet over the peninsula (Clarke 1984, Noonan and Smith 1986, Smith and Noonan 1998, Menhofer *et al.* 1997a, b, Goler and Reeder 2004, Thomsen and Smith 2006; see also the reviews by Smith 1988, Christie 1992, and Reeder and Smith 1998). Striking roll clouds, known in Australia as northeasterly morning glories, are observed regularly as moist low-level air is lifted and cooled adiabatically in the crest of the individual bore waves and warms as it descends in the wave troughs that follow.

#### 4 Event 2

The second cold front, Event 2, passed through Mount Isa just after midnight, at about 0020 EST 17 September. There are three important differences between the Events 1 and 2. First, Event 2 passed rapidly across the observational network towards the gulf in the late evening

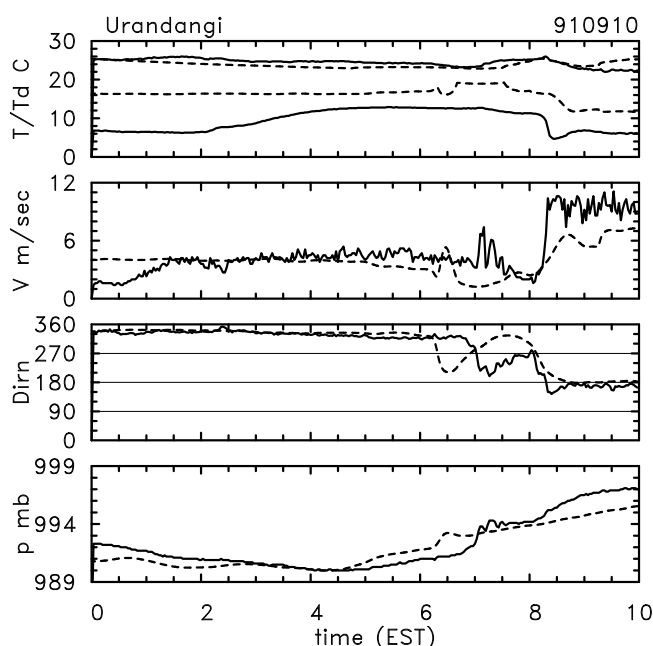


Figure 9. Event 1. Observed time series of temperature  $T$  and dew-point temperature  $T_d$ , wind speed  $V$ , wind direction at a height of 2 m  $Dirn$ , and surface pressure  $p_s$  at Urandangi between 0000 and 1000 EST on 10 September. Reproduced from Smith *et al.* (1995). The dashed curves show the corresponding curves from the MM5 inner domain, except that the wind data are extracted at 10 m.

and early hours of the morning. In contrast, Event 1 reached Mount Isa mid-morning, weakened and decelerated, finally reaching the gulf in the early hours of the following morning. Second, sharp temperature falls accompanied the passage of Event 2, whereas the temperature changed little with the arrival of Event 1. Third, an amplitude-ordered family of solitary waves was generated and propagated ahead of Event 1. In contrast, the undular bore that developed with Event 2 did not separate from the cold front until after sunrise, when front began to weaken. The brief analysis presented now focusses mainly on the differences between the two events.

#### 4.1 Synoptic environment for Event 2

The ECMWF analyses at 2200 EST 16 September is shown in Fig. 10. The synoptic environment is very similar to Event 1 (Fig. 1). Indeed, the synoptic environment is similar to all the subtropical cold fronts studied in the four field experiments held in the region. A high to the west and a weak low centred on the southeastern coastline directs a cold southerly airflow across the central part of the continent. The cold front (Event 2) is oriented southeast to northwest from the northern part of the low and along the northern boundary of the high. A heat trough is located to the north and parallel to the cold front.

#### 4.2 Mesoscale structure and frontogenesis during Event 2

After sunset, as the turbulent mixing weakens, the low-level winds accelerate toward the heat trough. Figures

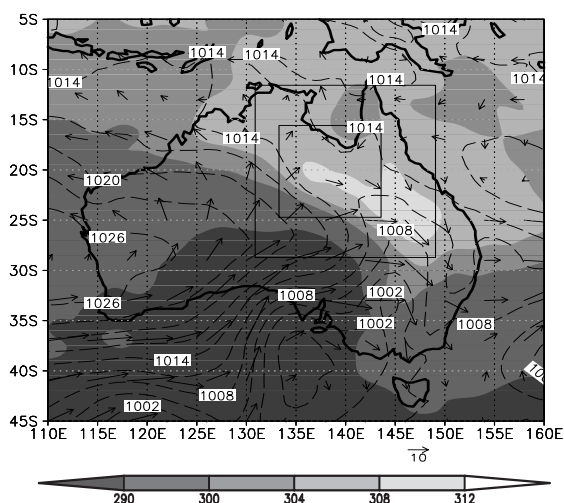


Figure 10. Event 2. ECMWF analyses at 2200 EST 16 September. MSLP (dashed lines), horizontal wind vectors and virtual potential temperature (shaded) at 850 mb. Contour intervals are 3 mb and 4 K. The two boxes centred over northeastern Australia show the outer and inner domains used in the simulations with MM5.

11 shows the potential temperature, horizontal divergence and horizontal wind fields at 2100 EST 16 September on the  $\sigma = 0.995$  surface and on the outer grid. At this time, two principal lines of elevated relative vorticity lay northwest to southeast across the middle of the domain. The more northeasterly of the two lines marks the northeastern side of heat trough. The more southwesterly of the two lines marks the cold front, and the two lines bound a tongue of warm air. Although not shown, both lines are accompanied by pronounced changes in the equivalent potential temperature. Strong southwesterlies and cold air lie to the southwest of the cold front. Subsequently, the cold front strengthens and accelerates, overtaking the first line and evolving into a propagating bore (Section 4.3). In the northern part of the domain at 2100 EST another line of elevated relative vorticity, aligned perpendicular to the low-level flow, corresponds to the sea breeze front, and a northeasterly morning glory is located over Cape York Peninsula.

Cross sections of the potential temperature and the terms that contribute to the frontogenesis function (Eq. 1) at 2100 EST 16 September are shown in Fig. 12. The tilting term is not plotted as its contribution is insignificant. In the plane of the vertical cross section, the cold front, as defined by the second line of vorticity, is located at about 400 km. The first, more northeasterly, line of vorticity is located at about 580 km along the cross section at the southwestern edge of a low-level cool anomaly. The sea breeze front is at about 750 km. The contribution to the frontogenesis function from deformation and convergence is large and positive through a depth of 1–2 km in the neighbourhood of the front (Fig. 12b). It is strong also in shallower layers centred on the heat trough, the first line of vorticity, and the sea breeze front. The diabatic contribution to the frontogenesis function is more complicated than that from deformation and convergence and

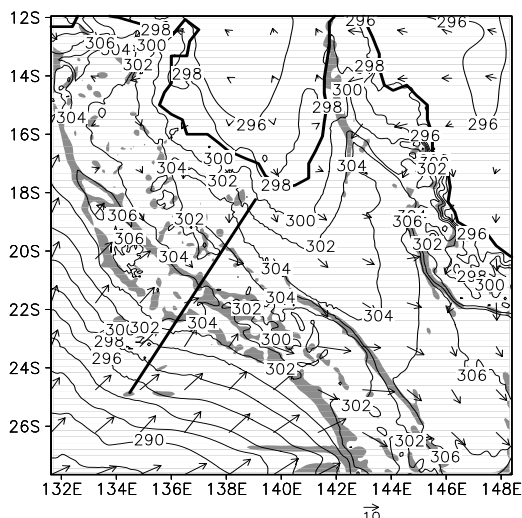


Figure 11. Event 2. Potential temperature and horizontal wind vectors on the  $\sigma = 0.955$  surface from the MM5 outer domain at 2100 EST, 17 September. Contour interval for potential temperature is 2 K. The arrow below each panel indicates  $10 \text{ m s}^{-1}$ . Shading marks those regions where the magnitude of the cyclonic relative vorticity exceeds  $7.5 \times 10^{-5} \text{ s}^{-1}$  on the same  $\sigma$ -surface. The thick line marks the location of the vertical sections plotted in Fig. 12.

is much more variable in time and space (Fig. 12c). It contributes to frontolysis at the cold front through mixing, but is frontogenetic far ahead of the cold front where the model produces shallow cloud. The net result is that the frontogenesis function is large and positive in the lowest 1.5 km in the region of the cold front and in a deeper layer above first line of vorticity (Fig. 12a). Between the two lines, the frontogenesis is function is negative. The frontogenesis function is large and positive also at the at the leading edge of the sea breeze.

#### 4.3 Comparison between the observations and simulation of Event 2 on the inner grid

Figure 13 shows time-height cross sections of potential temperature from the radiosonde ascents made at Mount Isa and from the corresponding model profiles. While a well-mixed layer forms during the day in both the model and observations, there is a large discrepancy in their depths. The depth of the mixed layer in the model is not much more than 2 km deep whereas the observations show that it is closer to 3.5 km. As in Event 1 the model fails to capture the very strong inversions observed at the top of the mixed layer and capping the cold, postfrontal air. The sensitivity of the depth of the mixed layer to the soil moisture was checked by rerunning MM5 with the soil moisture data from the Australian Bureau of Meteorology's limited area forecast model, which is drier than that from the ECMWF analyses. In this case, the mixed layer depth increased by only a few hundred metres. An intense, but shallow radiation inversion is observed to form beneath a deep well mixed-layer prior to the arrival of the front. The model simulation produces the same features, although they are weaker and more

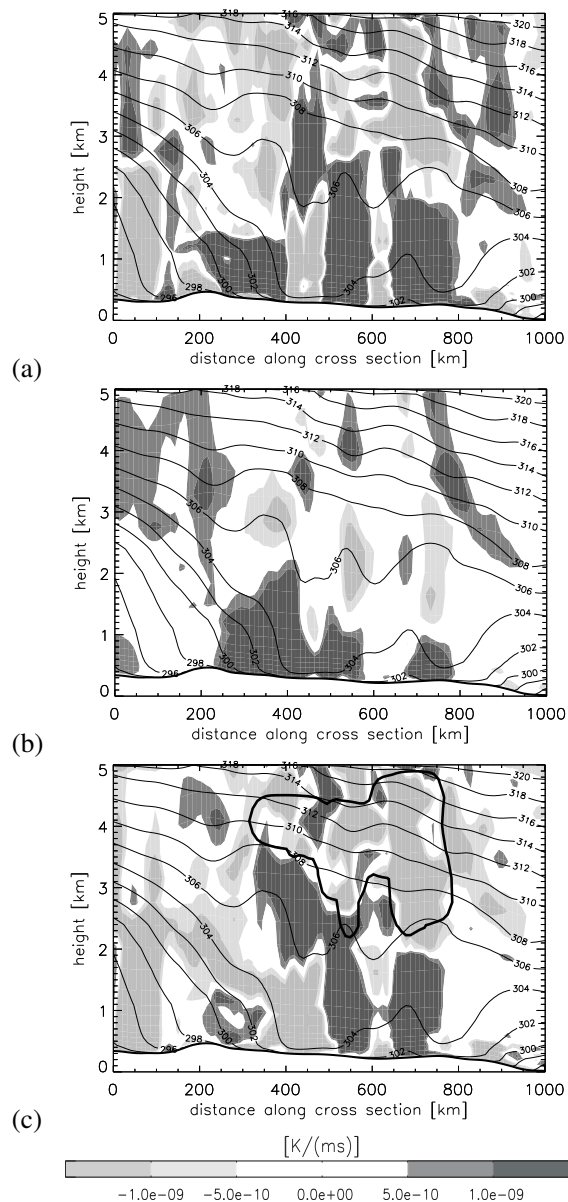


Figure 12. Event 2. Vertical cross section of the potential temperature and contributions to the frontogenesis function from the MM5 outer domain at 2100 EST 16 September along the line marked in Fig. 11. (a) Frontogenesis function  $D|\nabla_h \theta|/Dt$ . (b) Convergence and deformation term  $-\frac{1}{2}|\nabla_h \theta| (D - E' \cos(2\beta))$ . (c) Differential diabatic heating term  $\mathbf{n} \cdot \nabla_h \dot{Q}$ . Contour interval for potential temperature is 2 K. Contour interval for frontogenesis is  $5 \times 10^{-10} \text{ K m}^{-1} \text{ s}^{-1}$ . In panel (c) the bold contour marks cloud.

diffuse. The modelled front arrives at Mt Isa about 2 hours earlier than observed. Both the observed and modelled fronts are shallow, no more than 1.5 km deep. The coldest air arrives at Mount Isa at about 0900 EST, after which time the potential temperature increases during the day as the warming associated with diabatic heating exceeds the cooling produced by the post-frontal advection of cold air. The model captures this effect also, but produces a stronger gradient at the leading edge of the cold air at 0600 EST. The pressure jump in the model is approximately 1 mb, which agrees reasonably well with the observations.

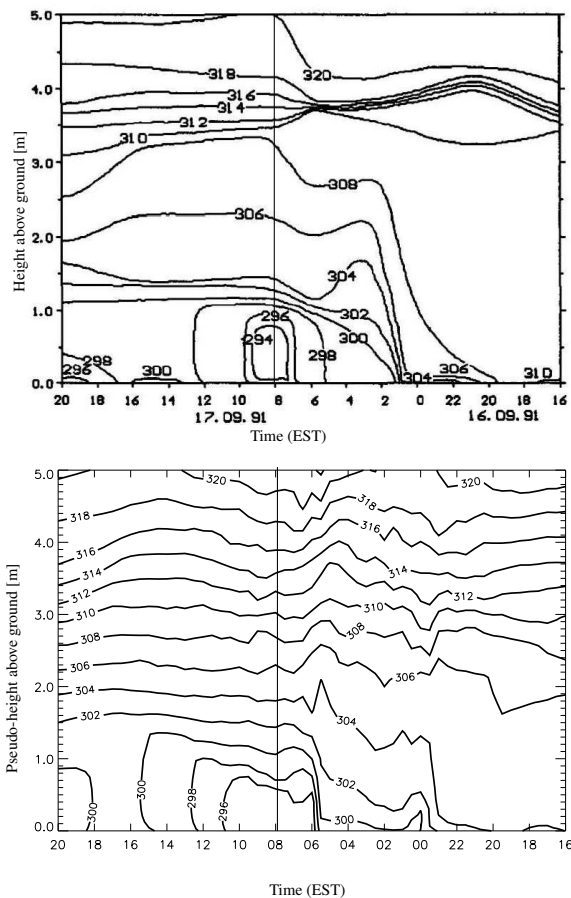


Figure 13. Event 2. (a) Time-height cross section of potential temperature from radiosonde ascents at Mount Isa. Time increases from right to left along the abscissa. The height in km is plotted along the ordinate. Contour interval is 2 K. Reproduced from Smith *et al.* (1995). The time of the frontal passage is indicated by a vertical line. (b) Time-height cross section of potential temperature from the MMS5 inner domain. Contour interval is 2 K. Pseudo-height in km is plotted along the ordinate.

#### 4.4 Development of the bore

Figures 14 and 15 show the modelled fields at 0600 EST. Plotted are the potential temperature, divergence and horizontal wind on the  $\sigma = 0.955$  surface, and vertical cross sections of potential temperature and relative wind normal to the front. At this time, the cold front advances at  $11 \text{ m s}^{-1}$  and is oriented almost east-west. It is marked by a band of convergence, a wind shift from northeast to south, and the arrival of the cold air (Fig. 14). In the vertical cross sections (Fig. 15), the front is located at 130 km and propagates to the right into a low-level stable layer produced by radiative cooling and the decaying sea breeze circulation from the Gulf of Carpentaria. The front is accompanied by a shallow cold pool immediately to the rear of the front and strong upward motion, and has features in common with a propagating undular bore. For example, the isentropes comprising the low-level stable layer are displaced sharply upward through a depth of about 1 km with the arrival of the front, while behind the front the isentropes undulate. The bore is not confined to the surface, but extends to a height of more than 3 km,

and the low-level relative inflow is every negative at its leading edge, which is also one of the properties of a bore. The bore formation is consistent with observations of a southerly morning glory that reached Burketown ( $139.5^\circ\text{E}$ ,  $17.7^\circ\text{S}$ ), located on the southeastern coastline of the Gulf of Carpentaria, at 0638 EST 17 September. This disturbance propagated at a speed of  $15.3 \text{ m s}^{-1}$  from a direction of  $205^\circ$  and was marked by a pressure jump of 1.4 mb. The NOAA-12 AVHRR visible satellite image at 0720 EST (Fig. 16) shows a pair of wave clouds propagating ahead of a field of shallow cumuli, which presumably marks the cold air.

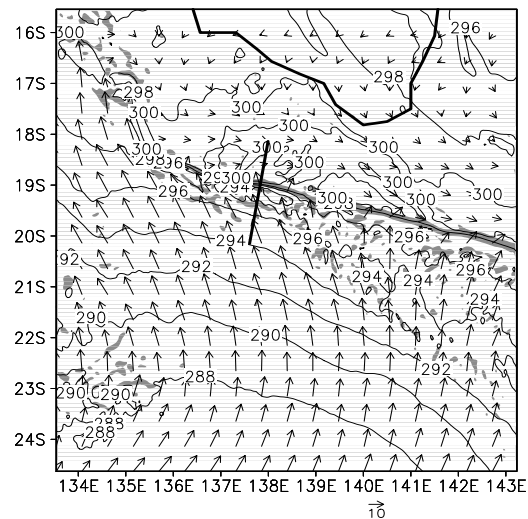


Figure 14. Event 2. Potential temperature and horizontal wind vectors on the  $\sigma = 0.955$  surface from the MMS5 inner domain at 0600 EST 17 September. Contour interval for potential temperature is 2 K. The arrow below each panel indicates  $10 \text{ m s}^{-1}$ . Shading marks those regions where the convergence exceeds  $1.5 \times 10^{-4} \text{ s}^{-1}$  on the same  $\sigma$ -surface. The thick line marks the location of the vertical section plotted in Fig. 15

#### 5 A comparison of the bores in Event 1 and Event 2

It is common for strong fronts to be interpreted locally as steady gravity currents (see Smith and Reeder 1988 and references therein). Haase and Smith (1989) reported a series of numerical experiments in which a gravity current advances into an environment that is neutrally stratified above a shallow, stable layer. In this configuration the key nondimensional parameter controlling the behaviour of the flow is  $\mu = c_0/c_{gr}$ . Here  $c_0 = 2Nh/\pi$  is the phase speed at which the small amplitude waves propagate on the stable layer,  $c_{gr}$  is the speed of the gravity current,  $N$  is the Brunt-Väisälä frequency in the stable layer ahead of the gravity current, and  $h$  is the depth of the stable layer. In the experiments of Haase and Smith, the gravity current head breaks away from the flow that advects cold fluid towards it and advances as a horizontal roll vortex. When the stable layer is sufficiently deep and strong to enable waves to propagate faster than the speed of the gravity current, the roll vortex evolves into a large-amplitude solitary-wave-like disturbance that propagates

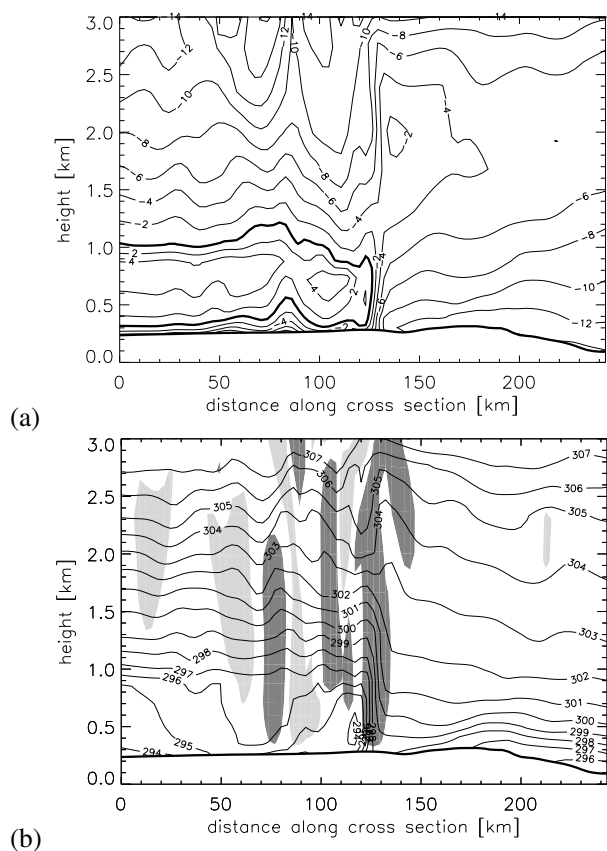


Figure 15. Vertical cross sections from the MM5 inner domain. Event 2 at 0600 EST 17 September. (a) Potential temperature and vertical motion. Contour interval for potential temperature is 1 K. Dark shaded regions represent vertical wind speeds greater than  $10 \text{ cm s}^{-1}$ . Light shaded regions represent vertical wind speeds less than  $-10 \text{ cm s}^{-1}$ . (b) Relative horizontal wind speed in the plane of the cross section  $u_n - c$ , where  $c = 11 \text{ m s}^{-1}$ . The bold line marks the  $0 \text{ m s}^{-1}$  contour.

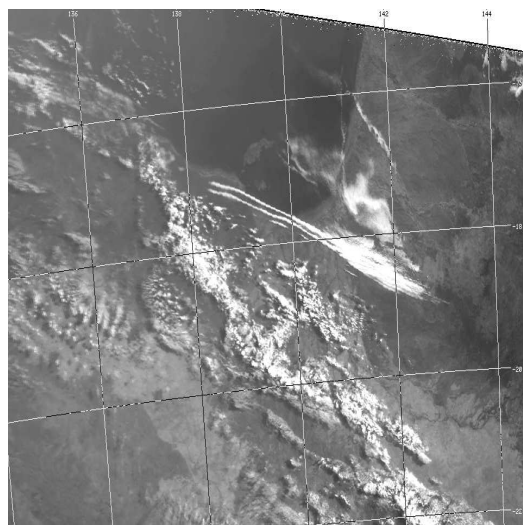


Figure 16. Event 2. NOAA-12 Advanced Very High Resolution Radiometer (AVHRR) visible satellite image at 0730 EST 17 September 1991. Reproduced from Smith *et al.* (1995).

ahead of the gravity current on the stable layer. In contrast, when the stable layer is comparatively shallow or weak,

the gravity current head becomes wavelike, but the waves remain attached to the gravity current and advect a small volume of cold air. The first case is said to be subcritical and the second case supercritical. Haase and Smith found that the transition from subcritical to subcritical flow occurred at about  $\mu = 0.7$ . The transition point is less than one because, according to weakly nonlinear theory, the phase speed of the waves which propagate on the stable layer increases with increasing amplitude.

The two paradigms reported by Haase and Smith (1989) appear to be relevant to Events 1 and 2. However, Haase and Smith used an empirical formula to determine  $c_{gr}$ , which is probably not appropriate here. For this reason and for simplicity, we define  $\mu = c_0/U_f$ , where  $U_f$  is the typical value of the horizontal wind in the cold air immediately behind the cold front. For Event 1 at 0600 EST (Fig. 7),  $\mu = 0.3 \pm 0.1$ . Like the subcritical case of Haase and Smith, the solitary-wave-like disturbance separates from the cold front and propagates ahead of it on the stable layer in both the model and the observations (Figs. 7 and 9). In contrast, at 0600 EST for Event 2,  $\mu = 0.9 \pm 0.3$  (Fig. 15). This event produced a particularly pronounced bore, which, in agreement with the observations and the calculation of the  $\mu$ , remained attached to the cold front, advecting cold air and developing a series of large-amplitude waves at its leading edge. Event 2 is similar to the Haase and Smith's supercritical case. The uncertainty attached to the calculations of  $\mu$  arises because of the difficulties in determining  $U$ ,  $N$  and  $h$  in a time varying, spatially complex flow. The likely errors in  $\mu$  have been estimated graphically.

In a steady, idealised gravity current, dense fluid is advected towards the head. Consequently, the low-level flow behind the head, normal to the direction of propagation,  $u_n$ , exceeds the translation speed of the head,  $c$ , so that  $u_n - c > 0$ . In contrast, the low-level flow behind an idealised, steadily propagating bore is less than the translation speed, so that  $u_n - c < 0$ . At 0200 EST 10 September,  $u_n - c_c > 0$  to the south of the front (Fig. 17a), where  $c_c$  is the speed of the convergence line at the leading edge of the front. Positive relative flow implies that cooling accompanying the passage of the disturbance is produced principally by the advection of cold air from the southwest. From this perspective, the front has at least one of the characteristics of a steady gravity current. At this time Event 1 comprises a single change with the lines of maximum convergence, cyclonic relative vorticity and potential temperature gradient almost coincident. Six hours later Event 1 has separated into two changes (Figs. 6 and 7). As discussed earlier, the first line has similarities with a solitary-wave-like disturbance, while the second line, which coincides with the onset of strong southerlies, has similarities with a propagating bore. The distribution of  $u_n - c_c$  is dramatically different at this time (Fig. 17b). The relative flow is almost everywhere negative, which means that the leading disturbance moves faster than the wind in the direction of translation. This is one of the characteristics of a wave, and it implies that any cooling

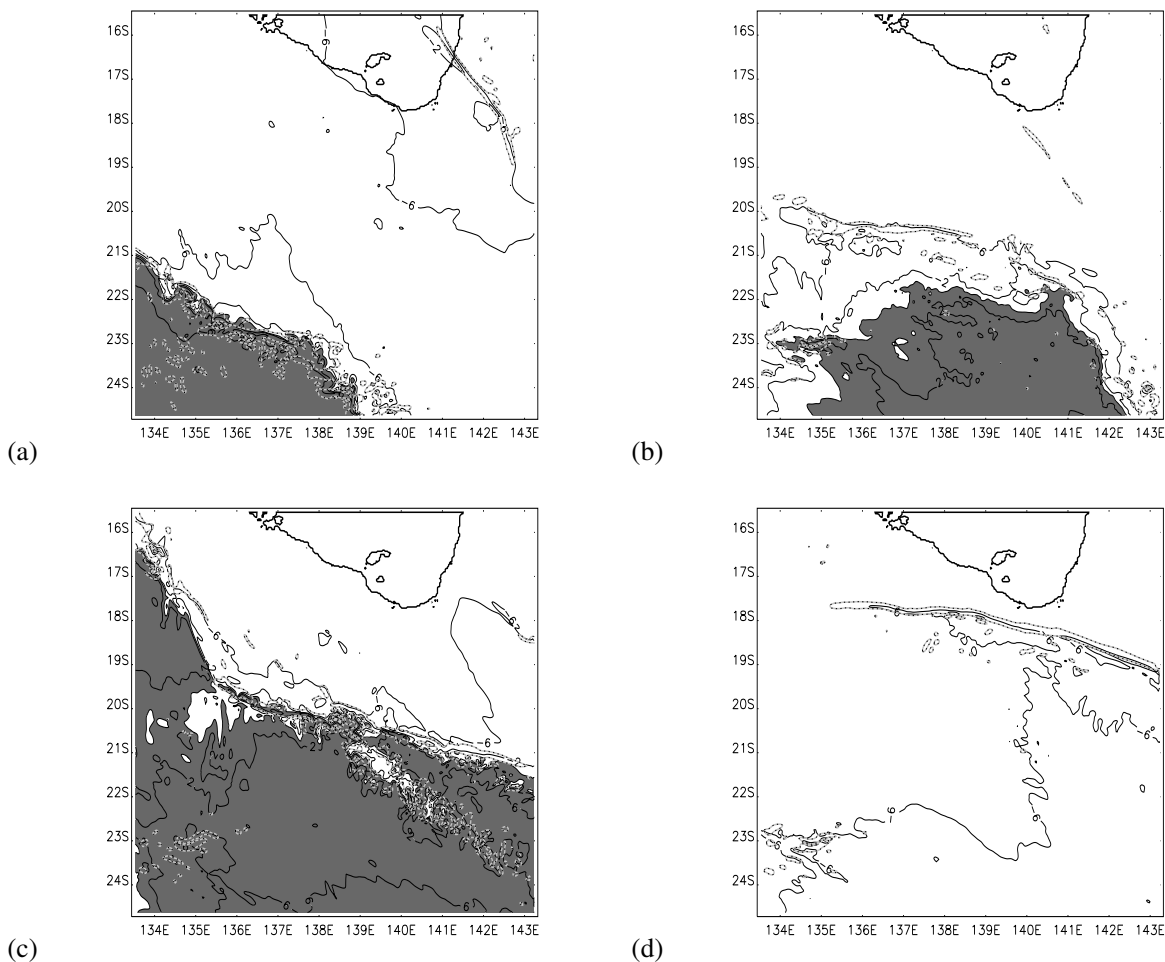


Figure 17.  $u_n - c_c$  on the  $\sigma = 0.955$  surface from the MM5 inner domain, where  $c_c$  is the speed of the leading convergence line. Event 1 at (a) 0200 EST and (b) 0900 EST 10 September, where  $c_c = 4.4 \text{ ms}^{-1}$  and  $c_c = 11.0 \text{ ms}^{-1}$  respectively. Event 2 at (c) 0300 EST and (d) 0900 EST 17 September, where  $c_c = 8.8 \text{ ms}^{-1}$  and  $c_c = 13.2 \text{ ms}^{-1}$  respectively. Shading indicates those regions where the relative flow is positive.

must be produced principally as air parcels are lifted and adiabatically cooled at the leading edge of the disturbance.

Likewise, for Event 2, the model shows that between 0300 and 0900 EST 17 September the relative flow changes radically (Fig. 17c and d). Behind the leading edge of the cold front at 0300 EST, the flow in the direction of the disturbance is almost everywhere faster than the disturbance itself ( $u_n - c > 0$ ), indicating that cold air advection is responsible for the cooling associated with the passage of the front. In contrast, there are only small regions of positive relative flow at 0900 EST, which is consistent with the interpretation that the leading disturbance has transformed into a bore ( $u_n - c < 0$ ) as it accelerates ahead of the original cold front. Although not shown, the original cold front weakens rapidly after sunrise and is hardly detectable by 0900 EST.

Caution is needed when interpreting plots of  $u_n - c$  as the condition  $u_n - c < 0$  does not by itself demonstrate that the leading change line is a solitary wave or propagating bore. This is because under certain circumstances, cold fronts may propagate, in which case  $u_n - c < 0$  also (Reeder and Smith, 1986, 1987, 1988, Smith and Reeder

1988). However, both Events 1 and 2 developed many of the structural characteristics of solitary waves or propagating bores, including a sharp vertical isentropic displacement followed by a series of undulations in the wind and potential temperature. Thus, it appears that, in the cases examined, the change in sign of  $u_n - c$  signals a fundamental change in the dynamics of the cold front.

## 6 Conclusions

This study has examined the effect of strong diurnal heating and cooling on the structure and evolution of cold fronts in the Australian subtropics and has sought to explain the observations made during a series of field experiments. The paper has focussed on numerical simulations of the two main cold fronts documented during the 1991 Central Australian Fronts Experiment, which have provided a more complete picture of the structure and evolution of the fronts and bore-like disturbances at scales smaller than those observable by the instrument array available at the time. Notwithstanding the differences in the timing of the cold front and in the depth of

the mixed layer compared with observations, the model captured the main observed features of the cold fronts and bores, demonstrating the capability of MM5 initialised with the routine ECMWF analyses to forecast the diurnal evolution of subtropical cold fronts. The contributions to explaining the observations are listed below.

Cold fronts in the Australian subtropics are observed to decelerate and rapidly weaken during the day, often becoming stationary and difficult to detect by the routine observational network. Our modelling study has shown that:

- While the daytime cross-isobaric flow towards the trough produces deformation and convergence in the boundary layer, the enhanced daytime turbulent stress acts to decelerate the low-level winds, the net result being a reduction of the deformation and convergence.
- Although the low-level wind field still acts to strengthen cold fronts during the day, they ultimately weaken and stall because the frontogenetic effect of deformation and convergence is outweighed by the frontolytic effect of daytime radiative heating and the associated turbulent mixing.
- Daytime turbulent mixing is frontolytic because the air in contact with the heated surface is rapidly mixed through the boundary layer, warming it at a rate which is inversely proportional to the depth of the boundary layer. Consequently, the cold side of the front warms faster than the warm side as the mixed layer is shallower in the cold air.

The cold fronts are observed to rapidly redevelop and accelerate at night once the boundary layer turbulence subsides. Our modelling study has shown that after sunset the low-level winds accelerate towards the centre of the trough. As the low-level winds strengthen, so do the contributions made to frontogenesis by deformation and convergence.

Observations have shown that subtropical cold fronts are shallow. Our modelling study indicates that this is because the mechanisms that lead to frontogenesis are confined to the boundary layer.

Observations have shown also that subtropical fronts invariably produce bores overnight. Our modelling study has shown that:

- Large regions of positive flow relative to the front develop behind the front following periods of frontolysis.
- After a period of strong frontogenesis during the night, large and abrupt vertical displacements of the isentropes form at the leading edge of the front together with regions of negative flow relative to the motion of these jumps. These results support the interpretation that the isentropic displacements are associated with propagating bores.
- The model reproduces the bore-like structure observed to develop during the early hours of the morning as the front strengthens and encounters the

developing radiation inversion and cool air advected inland by the sea breeze from the Gulf of Carpentaria. In agreement with the observations, the bore propagates ahead of the airmass change and develops a series of large-amplitude waves at its leading edge.

While the sequence of events described here is common over the Australian interior, it is not known how frequent it is elsewhere. Understanding the behaviour of cold fronts as they advance into subtropics in other parts of the world, such as over north Africa, remains a topic for further research.

### Acknowledgement

We are grateful to the ECMWF for providing analysis data. The first author gratefully acknowledges receipt of a research scholarship from the University of Munich, which supported this study, as well as a Rupert Ford Travel Award from the Royal Meteorological Society, which enabled him to visit research facilities in Australia, where part of this work was conducted.

### References

- Arnup SJ, Reeder MJ. 2007 The diurnal and seasonal variation of airmass boundaries in the Australian region. *Mon. Wea. Rev.*, **135**, 2995-3008
- Clarke RH. 1984 Colliding sea-breezes and the creation of internal atmospheric bore waves: two dimensional numerical studies. *Aust. Meteor. Mag.*, **32**, 207-226
- Christie DR. 1992 The morning glory of the Gulf of Carpentaria: A paradigm for non-linear waves in the lower atmosphere. *Aust. Meteor. Mag.*, **41**, 21-60
- Deslandes R, Reeder MJ, Mills G. 1999 Synoptic analyses of a subtropical cold front observed during the 1991 Central Australian Fronts Experiment. *Aust. Meteor. Mag.*, **48**, 87-110
- Dudhia J. 1989 Numerical study of convection observed during the winter monsoon experiment using a mesoscale two-dimensional model. *J. Atmos. Sci.*, **46**, 3077-3107
- Goler RA, Reeder MJ. 2004 The generation of the morning glory. *J. Atmos. Sci.*, **61**, 1360-1376
- Goler RA, Reeder MJ, Smith RK, Arnup S, Richter H, Keenan T, May P. 2006: Low-level convergence lines over northern Australia. I. The North Australian Cloud Line. *Mon. Wea. Rev.*, **134**, 3092-3108
- Grell GA. 1993 Prognostic evaluation of assumptions used by cumulus parameterizations. *Mon. Wea. Rev.*, **121**, 764-787
- Grell GA, Dudhia J, Stauffer D. 1995 A description of the 5th generation Penn State/NCAR mesoscale model (MM5). *Technical Report 398*, NCAR
- Haase SP, Smith RK. 1989 The numerical simulation of atmospheric gravity currents. Part II: environments with stable layers. *Geophys. Astrophys. Fluid Dyn.*, **46**, 35-51
- Hong SY, Pan HL. 1996 Nonlocal boundary layer vertical diffusion in a medium-range forecast model. *Mon. Wea. Rev.*, **124**, 1322-2399
- Hoskins, BJ, FP Bretherton 1972 Atmospheric frontogenesis models: Mathematical formulation and solution. *J. Atmos. Sci.*, **29**, 11-37
- Keyser D, Reeder MJ, Reed RJ. 1988 A generalization of Petterssen frontogenesis function and its relation to vertical motion. *Mon. Wea. Rev.*, **116**, 762-780
- May PT. 1995 The Australian nocturnal jet and diurnal variation of the boundary layer winds over Mt Isa in northeastern Australia. *Quart. J. Roy. Meteor. Soc.*, **121**, 987-1003
- Menhofer A, Smith RK, Reeder MJ, Christie DR. 1997a Morning Glory disturbances and the environment in which they propagate. *J. Atmos. Sci.*, **54**, 1712-1725

- Menhofer A, Smith RK, Reeder MJ, Christie DR. 1997b The bore-like character of three morning glories observed during the Central Australian Fronts Experiment. *Aust. Meteor. Mag.*, **46**, 277-285
- Noonan JA, Smith RK. 1986 Sea breeze circulations over Cape York Peninsula and the generation of Gulf of Carpentaria cloud line disturbances. *J. Atmos. Sci.*, **43**, 1679-1693
- Pagowski, M, PA Taylor, 1998 Fronts and boundary layer - Some numerical studies. *Bound. Lay. Meteor.*, **89**, 469-506
- Petterssen S. 1936 Contribution to the theory of frontogenesis. *Geophys. Publ.*, **11(6)**, 1-27
- Preissler MA, Reeder MJ, Smith RK. 2002 A case study of a heat low over central Australia. *Aust. Meteor. Mag.*, **51**, 155-163
- Reeder MJ, Smith RK. 1998 Mesoscale Meteorology. Meteorology of the Southern Hemisphere. Eds. D. Vincent and D.J. Karoly. *American Meteorological Society*, 201-241
- Reeder MJ, Christie DR, Smith RK, Grimshaw R. 1995 Interacting morning glories over northern Australia. *Bull. Amer. Meteor. Soc.*, **76**, 1165-1171
- Reeder MJ, Smith RK. 1998 Mesoscale Meteorology. Meteorology of the Southern Hemisphere. Ed. D.J. Karoly and D.G. Vincent. *Amer. Meteor. Soc.*, 201-241
- Reeder MJ, Tory KJ. 2005 The effect of the continental boundary layer on the dynamics of fronts in a two-dimensional model of baroclinic instability. Part II. Surface heating and cooling. *Quart. J. Roy. Meteor. Soc.*, **131**, 2409-2429
- Reeder MJ, Smith RK, Deslandes R, Tapper NJ, Mills GA. 2000 Subtropical fronts observed during the 1996 Central Australian Fronts Experiment. *Aust. Meteor. Mag.*, **49**, 181-200
- Smith RK. 1988 Travelling waves and bores in the lower atmosphere: the "Morning Glory" and related phenomena. *Earth Sci. Rev.*, **25**, 267-290
- Smith RK, Ridley R. 1990 Subtropical continental cold fronts. *Aust. Meteor. Mag.*, **38**, 191-200
- Smith RK, Noonan JA. 1998 On the generation of low-level mesoscale convergence lines over north-eastern Australia. *Mon. Wea. Rev.*, **126**, 167-185
- Smith RK, Reeder MJ, Tapper NJ, Christie DR. 1995 Central Australian cold fronts. *Mon. Wea. Rev.*, **123**, 19-38
- Smith RK, Reeder MJ, May P, Richter H. 2006 Low-level convergence lines over northern Australia. II. Southerly disturbances. *Mon. Wea. Rev.*, **134**, 3109-3124
- Thomsen GL, Smith RK. 2006 Simulations of low-level convergence lines over northeastern Australia. *Quart. J. Roy. Meteor. Soc.*, **132**, 691-707
- Weinzierl B, Smith RK, Reeder MJ, Jackson G. 2007 MesoLAPS predictions of low-level convergence lines over northeastern Australia. *Wea. and Forecasting*, **22**, 910-927